LERMA　Observatoire de Paris | PSL

Explaining Spectral Line Profiles in the Horsehead Nebula Using Cloud Surface Curvature

Student
Ducheng Lu

Supervisors
Franck Le Petit (LERMA)
Emeric Bron (LERMA)

Jan 2025

Contents

Abstract

Context.
Aim.
Methods.
Results.

Abstract

Contexte.
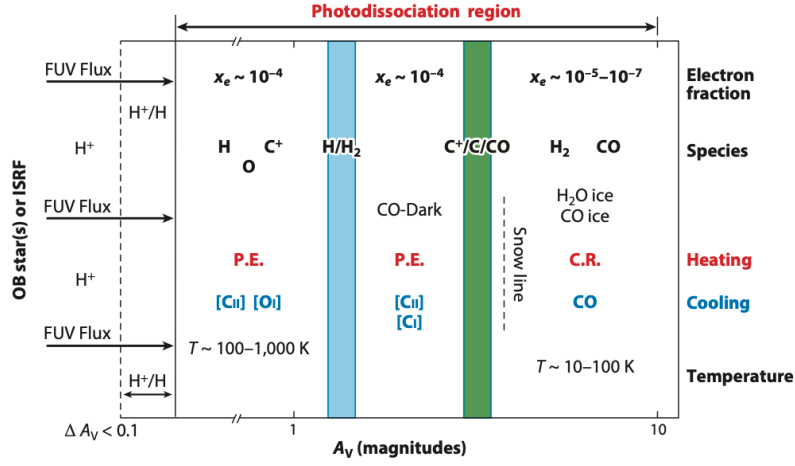*Objectif.*
Méthodes.
Résultats.

Figure 1: Schematic of a photodissociation region as a function of visual extinction A_V. Reprinted from Wolfire et al. (2022).

1 Introduction

The interstellar medium (ISM) is composed of gas and dust between stars in galaxies. The ISM is site of star formation and takes up around $\sim 10\%$ of total baryonic mass cite Drain2011. In return, the radiation field produced by stars is responsible for the heating the gas and dust that cool in bright line and continuum emission. These emission lines provide information about the physical conditions inside the ISM, such as the temperature, density and chemical composition.

Models have long been developed to help us interpret these

The 1D slab geometry may not be approprioate in some cases, and the curvature of the PDR region needs to be taken into account in order to reproduce the line profiles. A common technique is to use a time-dependent hydrodynamic simulation to obtain the density and velocity fields and then to postprocess it with a PDR code to obtain the steady-state chemical abundances and thermal equilibrium gas temperature (e.g., Levrier et al. 2012).

1.1 Photodissociation Regions (PDRs)

Photodissociation regions (PDRs) are regions where far-ultraviolet (FUV; $6\,\text{eV} < h\nu < 13.6\,\text{eV}$) radiation dominates the chemistry or heating processes(Tielens and Hollenbach 1985). PDRs span a wide range of incident FUV fluxes and densities, including all neutral gas in the interstellar medium (ISM) and molecular layers where FUV radiation drives molecule formation.

1.2 The Horsehead Nebula

In order to compare with observations, we need to convert the distance unit cm used the in `MeudonPDR` code into the arcsec unit used in observation,

$$\alpha['''] = \frac{d\,[\text{pc}]}{400\,\text{pc}} \frac{1\,\text{arcsec}}{1\,\text{rad}} \tag{1}$$

where $400\,\text{pc}$ (Menten et al. 2007; Schlafly et al. 2014) is the distance to the horsehead nebula.

Figure 2: Horsehead Nebula captured by the Hubble Space Telescope (HST) in 2013. The image was created from Hubble data from proposal 12812. Illustration Credit: NASA, ESA, and Z. Levay (STScI)
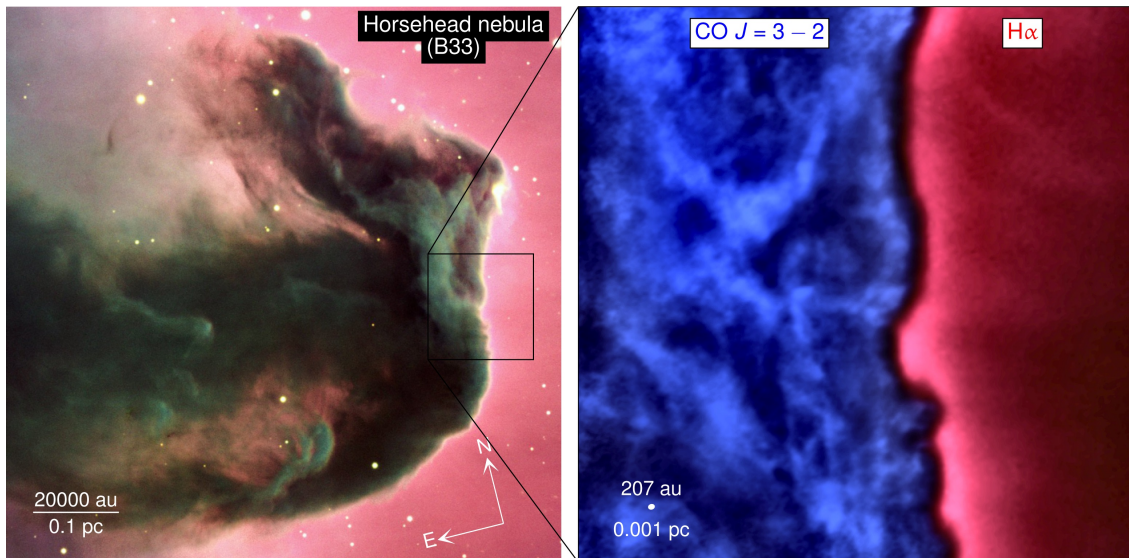

Figure 3: Multiphase view of the Horsehead nebula (Barnard 33). Reprinted from Hernández-Vera et al. (2023). Left: Composite color image of the Horsehead nebula observed with the VLT (ESO). Right: Zoomed-in view of the edge of the molecular cloud, imaged with ALMA in the CO $J = 3 - 2$ line emission (blue) and the 0.9 m KPNO telescope in the Hα line emission. The dark region represents the neutral atomic layer.
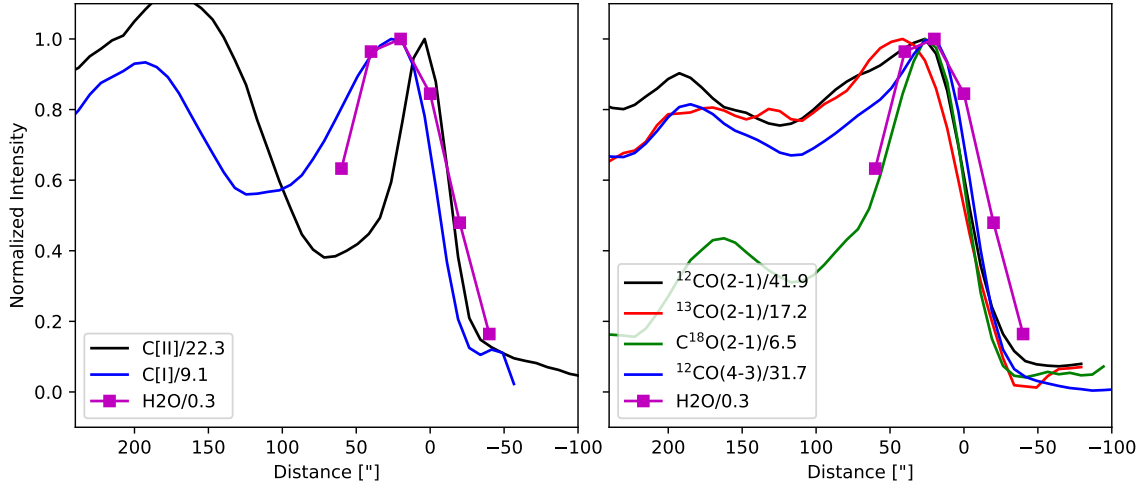
Figure 4: Observed line profiles of the Horsehead Nebula by Herschel HIFI. Reproduced from cite the original paper. ?The ^{13}CO lines has been removed due to bad weather condition during the observation.

2 Data

The observational data used in this study (Fig. 4) were obtained from the Heterodyne Instrument for the Far-Infrared (HIFI) (de Graauw et al. 2010) onboard the Herschel Space Observatory (Pilbratt et al. 2010). All data are convolved to the spatial resolution of the HIFI H_2O data, 38.1 arcsec. The observed molecular species were detected at specific wavelengths corresponding to transitions listed in Table 1.

Notation	Species	Upper Level	Lower Level	Frequency (GHz)
H_2O	H_2O	J=1, Ka=1, Kc=0	J=1, Ka=0, Kc=1	557.30
C[II]	C^+	2P J=3/2	2P J=1/2	1902.59
C[I]	C	3P J=1	3P J=0	492.02
^{12}CO (2-1)	CO	v=0, J=2	v=0, J=1	230.538
^{12}CO (4-3)	CO	v=0, J=4	v=0, J=3	461.041
^{13}CO (2-1)	^{13}CO	v=0, J=2	v=0, J=1	220.399
C^{18}O (2-1)	C^{18}O	v=0, J=2	v=0, J=1	219.560

Table 1: Parameters of transitions in the observation data used in this study.

3 Methods

3.1 The `MeudonPDR` code

A significant heterogeneity exists among the available PDR models, which differ in their geometry, physical and chemical structures, and model parameters. Röllig et al. (2007) suggest that the choice of a spedific code should depend on the physical and chemical processes implemented in the code, as well as the characteristics of the emission source.

In this project, I used the `MeudonPDR` code (Bron 2014; Bron et al. 2014, 2016; Goicoechea and Le Bourlot 2007; Gonzalez Garcia et al. 2008; Le Bourlot et al. 2012;
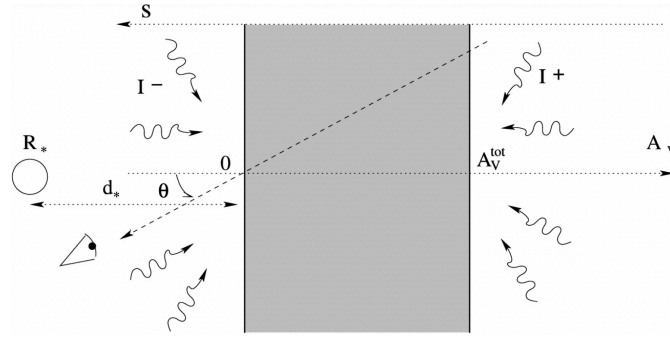
Figure 5: Scheme of the slab geometry of the `MeudonPDR` code. Reprinted from Le Petit et al. (2006).

Le Petit et al. 2006) to simulate the Horsehead Nebula. The `MeudonPDR` code models a stationary one-dimensional (1D) slab of gas and dust illuminated by an ultraviolet (UV) radiation field from one or both sides (Fig. 5). At each iteration, the code solves the UV radiative transfer in both the continuum and lines, followed by the chemical balance, and finally the level populations and thermal balance. The code outputs the level populations, the gas temperature, and the chemical abundances as a function of the depth into the cloud, with optional output of the radiation field. The physical parameters used to model the Horsehead PDR are summarized in Table 2.

Cloud size (A_V[1])	40
Proton density[2] (n_H)	$3 \times 10^4 - 3 \times 10^6 \, \text{cm}^{-3}$
Pressure[2] (P)	$1 \times 10^6 - 1 \times 10^7 \, \text{K cm}^{-3}$
ISRF	shape: Mathis[3], geometry: beam_isot[4]
ISRF scaling factor	$G_0^{\text{obs}} = 100$, $G_0^{\text{back}} = 0.04$[5]
UV radiative transfer method	FGK approximation, or
	exact H_2 self- and mutual shielding[6]
Turbulent velocity dispersion	$2 \, \text{km s}^{-1}$[7]
Extinction Curve	HD38087[8]
$R_V = A_V/E(B-V)$	5.50
$C_D = N_H/E(B-V)$	1.57×10^{22}

Table 2: Key physical parameters used to model the Horsehead PDR in the `MeudonPDR` code. [1]Visual extinction, $A_V \equiv 2.5 \log_{10}(I_V^0/I_V^{\text{obs}})$. [2]Proton density is used in constant density models, and pressure is used in constant pressure models(see Section 3.1.1). [3]Mathis et al. (1983). [4]Perpendicular on observer side, isotropic on back side. [5]In Habing units, as defined in Le Petit et al. (2006). [6] See Section. 3.1.2. [7]Only used in Doppler line broadening. [8]Fitzpatrick and Massa (1990). Other parameters use default values. More descriptions can be found in the `MeudonPDR` code documentation.

3.1.1 Constant Pressure vs. Constant Density

The density structure of a PDR model, whether it assumes constant density, constant pressure, or a user-defined density profile, can significantly influence the simulation results (Wolfire et al. 2022). As shown in Fig. 6 and Fig. 7, I compare the cloud structure computed with constant pressure and constant density assumptions, illustrating the differences in the resulting PDR structures. The values $n_H = 3 \times 10^5 \, \text{cm}^{-3}$ for the constant

density model and $P = 5 \times 10^6 \, \mathrm{K \, cm^{-3}}$ for the constant pressure model are based on Maillard (2023). In the constant pressure model, the transition from atomic to molecular hydrogen occurs at higher visual extinction (Fig. 6), and the total physical thickness of the cloud is larger (Fig. 7). The temperature profile in the constant pressure model is also more gradual. Additional comparisons between various constant density models and constant pressure models are provided in the appendix.

Observations of the Horsehead Nebula reveal a steep density gradient in the PDRs (Guzmán et al. 2011; Habart et al. 2005). Hernández-Vera et al. (2023) showed that constant density models fail to reproduce the observed structures, and neither do previously proposed density profile prescriptions. Furthermore, recent observations from ALMA and Herschel indicate that the warm layer of PDRs is indeed isobaric, with by relatively high thermal pressures (Bron et al. 2018; Goicoechea et al. 2016; Joblin et al. 2018; Maillard et al. 2021; Marconi et al. 1998; Wu et al. 2018). Based on these findings, I adopt a constant pressure model with $P = 5 \times 10^6 \, \mathrm{K \, cm^{-3}}$ for the subsequent analysis.
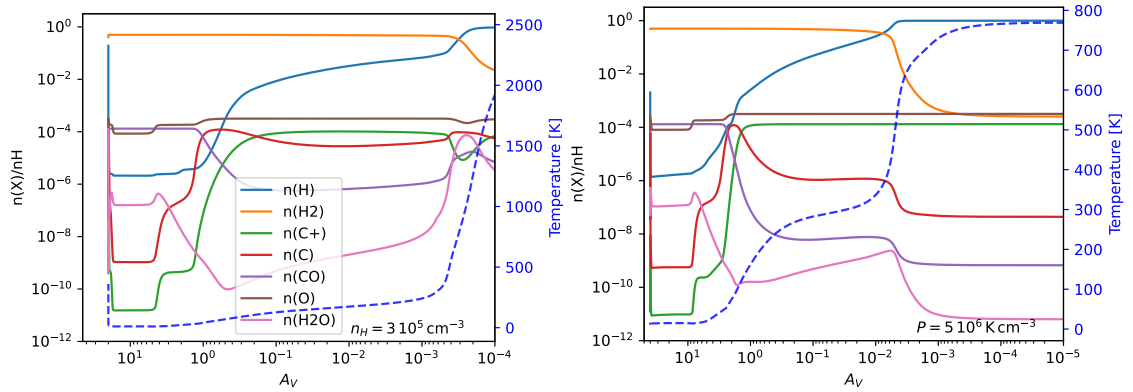

Figure 6: Comparison of the cloud structure computed with constant density $n_H = 3 \times 10^5 \, \mathrm{cm^{-3}}$ (left) and constant pressure $P = 5 \times 10^6 \, \mathrm{K \, cm^{-3}}$ (right), with a shared legend displayed in the left plot. All other parameters are the same as those listed in Table. 2.
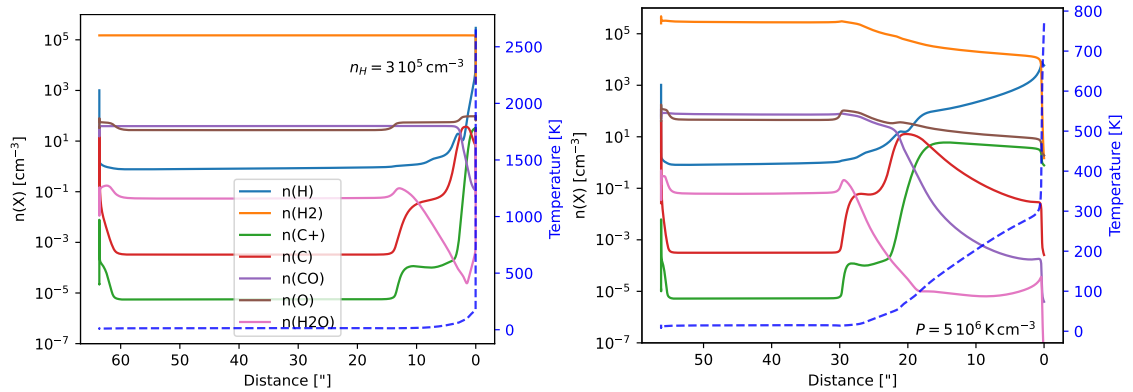

Figure 7: Similar to Fig. 6, but using physical units, with arcseconds as the distance unit and the densities represented by their actual values (not normalized by proton density).

3.1.2 Models with Exact Radiative Transfer of H$_2$

There are two options available in the MeudonPDR code for treating radiative transfer in the UV. The first is the FGK approximation (Federman et al. 1979), in which the self-shielding of H and H$_2$ molecules is treated approximately. Self-shielding occurs when

molecules absorb radiation in their own spectral lines, reducing the flux available to penetrate deeper into the cloud. However, the FGK approximation neglects mutual shielding, where the overlap and interaction of absorption lines between different species or multiple lines of the same species further attenuate the radiation field.
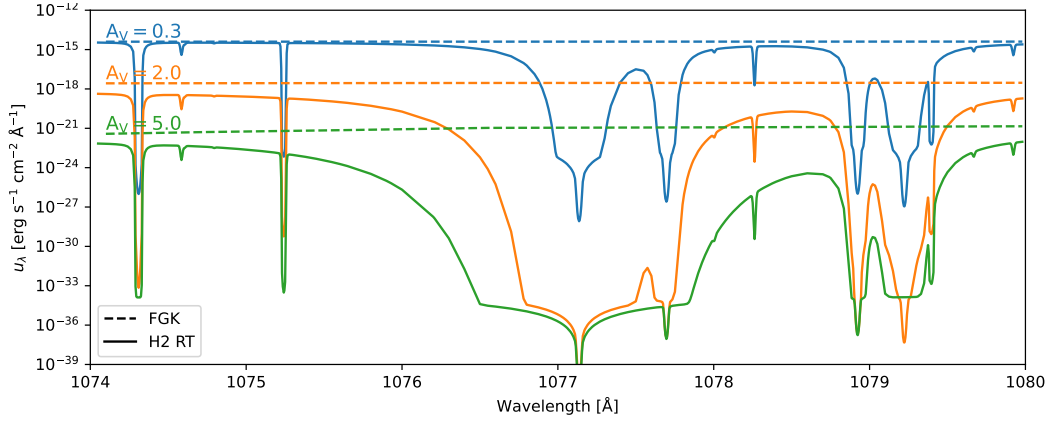

Figure 8: Comparison of the local energy density of the radiation field from 1074 Å to 1080 Å at visual extinction depths $A_V = 0.3$ (blue), $A_V = 2$ (orange), and $A_V = 5$ (green), for models computed using the FGK approximation (dashed lines) and the exact radiative transfer method (solid lines) including the 20 lowest H_2 absorption lines.

The second, more accurate approach is to solve the radiative transfer exactly. This method explicitly includes mutual shielding for a given number of energy levels of H, H_2, D, HD, CO, ^{13}CO, and $C^{18}O$, as detailed in Goicoechea and Le Bourlot ([2007]) and Gonzalez Garcia et al. ([2008]). For higher energy levels, the FGK approximation is retained, as their contributions are negligible due to their low populations.

Fig.[8] compares spectra from 1074 Å to 1080 Å at various visual extinction values for models computed using the FGK approximation and the exact radiative transfer method, demonstrating pronounced attenuation when applying the exact method of H_2 radiative transfer. Although computationally more intensive, the exact method enables a more accurate treatment of the UV radiation field, which subsequently influences the PDR structure. For instance, the exact method leads to increased attenuation of the radiation field, shifting the H/H_2 transition layer to lower extinction depths (Goicoechea and Le Bourlot [2007]), as illustrated in Fig.[9]. Furthermore, the enhanced attenuation from mutual shielding results in a lower temperature profile. To balance accuracy and computational efficiency, my model applies exact radiative transfer only to the 20 lowest energy levels of H_2, which are the primary contributors to the attenuation. how to explain the second bump occuring in the both cases?

3.1.3 Models with Surface Chemistry

In the ISM, direct gas-phase formation of molecules is very inefficient. Instead, molecules are formed on the surfaces of dust grains, which act as catalysts by providing a surface for adsorbed atoms to meet and react. The grains also absorb the excess energy released by the formation process, preventing dissociation that would otherwise occur in the gas-phase formation. The formation of H_2 is a key demonstration of the importance of this process, as the gas-phase formation rate of H_2 is much lower than the rate required to explain the observed abundance of H_2 in the ISM (Gould and Salpeter [1963]; Hollenbach and Salpeter [1971]). In addition to chemical reactions, dust grains also play
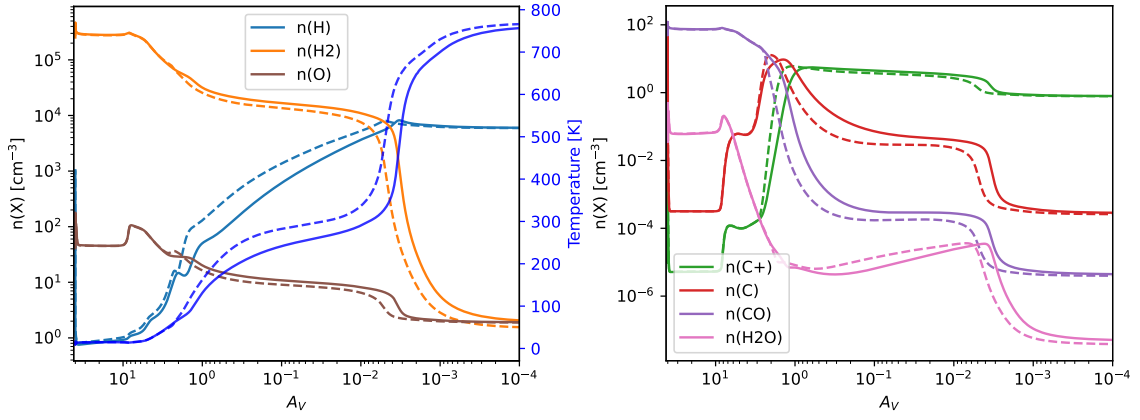
Figure 9: Comparison of temperature profile and abundances for models computed with (solid) and without (dashed) exact radiative transfer (RT) of H_2: H species and O (left), and C species, CO, and H_2O (right).

a role in the sublimation and freeze-out of molecules, leading to "jumps" or "drops" in molecular profiles at specific temperatures (Herbst and van Dishoeck 2009).
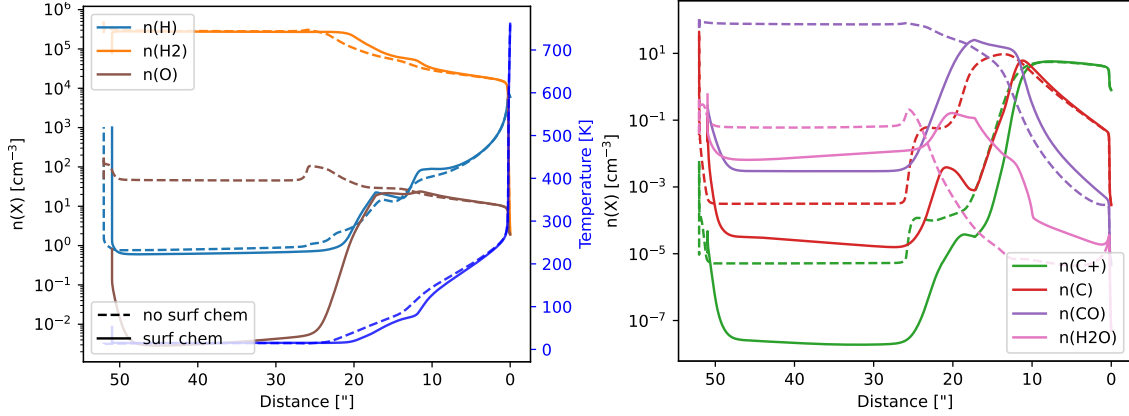

Figure 10: Comparison of temperature profile and abundances for models computed with (soid lines) and without (dashed lines) surface chemistry: H species and O (left), and C species, CO, and H_2O (right).

In Fig. 10, I compare the PDR models computed with and without surface chemistry. The inclusion of surface reactions leads to an earlier rise in the abundances of $n(H_2)$, $n(CO)$ and $n(H_2O)$ due to enhanced production on dust grain surfaces. At greater depths within the cloud, the abundances of almost all molecules decrease in the model with surface chemistry because of the freeze-out of molecules onto the dust grains. Grains also reduce the gas temperature, as they absorb the energy released during molecule formation, as shown in the left panel. Therefore, including surface chemistry in PDR models is crucial for accurately describing the molecular abundances and the gas temperature.

To summarize the model comparisons in this section, we will use the constant pressure model with exact radiative transfer of H_2 and surface chemistry to consider the curvature of the cloud's surface in the following sections.

3.2 Column Density in a Spherical Geometry

To model the curvature of the cloud, we treat the PDR region as the outermost shell of a fictitious spherical cloud, assuming plane-parallel geometry, as shown in Fig. 11. This approximation is valid when the curvature radius of the cloud's surface is relatively small compared to the radius of the cloud. For the models in this study, the physical depth of the PDR region is approximately $0.08\,\text{pc}$, which is significantly smaller than the curvature radius, as seen in Fig. 3, thereby justifying the use of plane-parallel geometry. Under this assumption, we consider all physical variables at a given distance from the cloud's surface to be equal to those computed by the `MeudonPDR` code model at the same distance from the cloud's edge.

The radius R of the fictitious spherical cloud is provided as an input parameter to the wrapper code. A line of sight (LoS) is defined by its impact parameter b, which measures the perpendicular distance from the LoS to the center of the cloud. From the output of the `MeudonPDR` code, the level number densities $n_X(d)$ are obtained as a function of the depth d into the cloud. In plane-parallel geometry, $n_X(d)$ gives the number density at a point located at a depth d from the spherical surface.

Figure 11: Scheme of the spherical, plane-parallel geometry. Curvature exaggerated for clarity.

The column density along a given LoS is determined by interpolating the number density at each depth d and then integrating along the LoS. To do this, we first compute the range of distances inside the PDR region along the LoS. The maximum half-distance s_{max} is given by:

$$s_{\text{max}} = \sqrt{R^2 - b^2}, \tag{2}$$

while the computation of the minimum half-distance s_{min} depends on whether the LoS penetrates beyond the PDR region (see Fig. 11):

$$s_{\text{min}} = \begin{cases} 0 & \text{if } b > R - d_{\text{PDR}}, \text{ LoS 1} \\ \sqrt{(R - d_{\text{PDR}})^2 - b^2} & \text{if } b < R - d_{\text{PDR}}, \text{ LoS 2} \end{cases}, \tag{3}$$

where d_{PDR} is the depth of the PDR region. Next, the distance s along the LoS is converted into the depth d from the cloud's surface. Using Pythagorean theorem, we can easily establish that $d = R - \sqrt{s^2 + b^2}$. The number density at each point along the LoS is then calculated as:

$$n_X(s) = f(R - \sqrt{s^2 + b^2}), \tag{4}$$

where $f(d)$ is the interpolated function of the level number density $n_X(d)$. Finally, the column density $N_X(b)$ for a given LoS with impact parameter b is obtained by integrating the number density along the LoS. By symmetry, the total column density is twice the integral over the half-LoS:

$$N_X(b) = 2 \int_{s_{\text{min}}}^{s_{\text{max}}} n_X(s')\mathrm{d}s'. \tag{5}$$

By considering the curvature of the cloud's surface, this column density allows for a more direct comparison with observations. However, this approach does not account for the absorption and emission processes occurring inside the cloud. For lines that are optically thick, the radiative transfer equation must be solved along the LoS to accurately reproduce the observed line profiles. This more detailed treatment will be addressed in the next section.
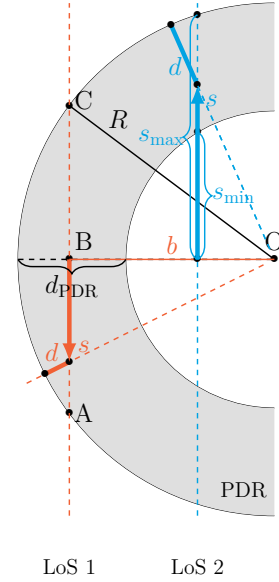
3.3 Radiative transfer equation

In the previous calculation of the column densities, we have made the assumption that all lines are optically thin; in fact, some of the lines can be optically thick, which explains the difference in the shape of the curve in observations for different lines in Fig 4.

To account for line extinction inside the cloud, we need to solve the radiative transfer equation along the LoS cite see, for example, Eq (1.67) Rybicki?:

$$\frac{\mathrm{d}I_\nu}{\mathrm{d}s} = A_{ul}n_u\frac{h\nu}{4\pi}\phi(\nu) + B_{ul}n_u\frac{h\nu}{4\pi}I_\nu\phi(\nu) - B_{lu}n_l\frac{h\nu}{4\pi}I_\nu\phi(\nu), \tag{6}$$

where n_u and n_l are the number densities of the upper and lower levels of the transition, respectively, h is the Planck's constant, ν is the frequency of the transition, and $\phi(\nu)$ is the line profile. We assume that the emission and absorption profiles are the same and we neglect scattering justify?. A_{ul}, B_{ul}, B_{lu} are the Einstein coefficients for this transition, which are related by the Einstein relation references

$$B_{ul} = \frac{c^2}{2h\nu_{ul}^3}A_{ul},\ g_lB_{lu} = g_uB_{ul}, \tag{7}$$

where g_u and g_l are the degeneracies of the upper and lower levels, respectively.

For consistency, we keep the same values for the Einstein coefficients as in the `MeudonPDR` code, which are taken from references?.

In the PDR, turbulences are the dominant line broadening process references? a bit more on line broadening in the intro?, in which case the line profile $\phi(\nu)$ is a Gaussian profile in the form references

$$\phi(\nu) = \frac{1}{\sigma_\nu\sqrt{2\pi}}\exp\left(-\frac{(\nu-\nu_0)^2}{2\sigma_\nu^2}\right), \tag{8}$$

where

$$\sigma_\nu = \frac{\sqrt{2}}{2}\Delta\nu_D,\ \Delta\nu_D = \frac{\nu_0}{c}\sqrt{\frac{2kT}{m} + v_{\text{turb}}^2}. \tag{9}$$

The turbulent velocity v_{turb} is a parameter in the `MeudonPDR` code, with a default value of $2\,\mathrm{km\,s^{-1}}$. T is the temperature, and m is the mass of the line-emitting species. For the mass we use the same value as the `MeudonPDR` code (as defined in , taken from Scientific Instrument Services (SIS) database? change name?

The line profile is normalized so that $\int_0^\infty \phi(\nu)\mathrm{d}\nu = 1$. In practice, we truncate the line profile at 5σ add a figure to demonstrate that this is reasonable for the lines concerned?, i.e., the normalization becomes

$$\int_{\nu_0-5\sigma}^{\nu_0+5\sigma} \phi(\nu)\mathrm{d}\nu = 1 \tag{10}$$

To solve the radiative transfer equation, we also need a background intensity I_0. For this we use the isotropic specific intensity on the observation side output by the `MeudonPDR` code, in the `_IncRadField.dat` file. add explanation that our implementation is only valid for isotropic radiation and explains why we couldn't implement a more generic background specific intensity.

The external radiation field in the `_IncRadField.dat` file is in units of $\mathrm{erg\,cm^{-2}\,s^{-1}\,sr^{-1}\,\AA^{-1}}$, so we need to convert the specific intensity in to $\mathrm{erg\,cm^{-2}\,s^{-1}\,sr^{-1}\,Hz^{-1}}$,

$$I_\nu|\mathrm{d}\nu| = I_\lambda|\mathrm{d}\lambda| \Rightarrow I_\nu = I_\lambda\left|\frac{\mathrm{d}\lambda}{\mathrm{d}\nu}\right| = I_\lambda\frac{c}{\nu^2} = I_\lambda\frac{\lambda^2}{c} \tag{11}$$

$$\lambda = \frac{c}{\nu} \Rightarrow d\lambda = -\frac{c}{\nu^2} d\nu \Rightarrow \left| \frac{d\lambda}{d\nu} \right| = \frac{c}{\nu^2} = \frac{\lambda^2}{c} \tag{12}$$

It is often more convenient to do a change of variable and integrate over optical depth

$$\frac{dI_\nu}{d\tau_\nu} = S_\nu - I_\nu, \tag{13}$$

with

$$\tau_\nu = \alpha_\nu ds, \; S_\nu = \frac{j_\nu}{\alpha_\nu} \tag{14}$$

$$\alpha_\nu = \frac{h\nu}{4\pi}\phi(\nu)(B_{lu}n_l - B_{ul}n_u) \tag{15}$$

$$j_\nu = A_{ul}n_u \frac{h\nu}{4\pi}\phi(\nu) \tag{16}$$

To test the solver, we first solve the radiative transfer with constant density profiles of both the lower and upper level, then the radiative transfer equation becomes

$$\frac{dI_\nu}{ds} = c_1 + c_2 I_\nu, \tag{17}$$

with

$$c_1 = A_{ul}n_u \frac{h\nu}{4\pi}\phi(\nu) = \text{cst}$$

$$c_2 = (B_{ul}n_u - B_{lu}n_l)\frac{h\nu}{4\pi}\phi(\nu) = \text{cst}.c$$

The analytical solution is

$$I_\nu(s) = (I_0 + \frac{c_1}{c_2})e^{c_2 s} - \frac{c_1}{c_2}. \tag{18}$$

For example, if we consider the CO transition from v = 0, J = 2 to v = 0, J = 1, with a constant density profile of $n_u = 2\,\text{cm}^{-3}$, $n_l = 2\,\text{cm}^{-3}$, $A_{ul} = 6.911 \times 10^{-7} s^{-1}$

- $h\nu/4\pi = 4.86234284e - 16$

- $A_{ul} = 6.911e - 07$

- $B_{ul} = 3825410.21021763$

-

3.4 Convolution

4 Results and Discussion

4.1 Cloud Surface Curvature

4.2 Line Profiles

5 Conclusions

References

Bron, E. (2014). "Stochastic processes in the interstellar medium". 2014PA077169. PhD thesis, 1 vol. (382 p.)

Bron, E., Le Bourlot, J., and Le Petit, F. (2014). "Surface chemistry in the interstellar medium. II. H_2 formation on dust with random temperature fluctuations". In: A&A 569, A100, A100. DOI: 10.1051/0004-6361/201322101.

Bron, E., Le Petit, F., and Le Bourlot, J. (2016). "Efficient ortho-para conversion of H_2 on interstellar grain surfaces". In: A&A 588, A27, A27. DOI: 10.1051/0004-6361/201527879.

Bron, E. et al. (2018). "Photoevaporating PDR models with the Hydra PDR Code". In: *arXiv e-prints*, arXiv:1801.01547, arXiv:1801.01547. DOI: 10.48550/arXiv.1801.01547.

de Graauw, T. et al. (2010). "The Herschel-Heterodyne Instrument for the Far-Infrared (HIFI)". In: A&A 518, L6, p. L6. DOI: 10.1051/0004-6361/201014698.

Federman, S. R., Glassgold, A. E., and Kwan, J. (1979). "Atomic to molecular hydrogen transition in interstellar clouds." In: ApJ 227, pp. 466–473. DOI: 10.1086/156753.

Fitzpatrick, E. L. and Massa, D. (1990). "An Analysis of the Shapes of Ultraviolet Extinction Curves. III. an Atlas of Ultraviolet Extinction Curves". In: ApJS 72, p. 163. DOI: 10.1086/191413.

Goicoechea, J. R. and Le Bourlot, J. (2007). "The penetration of Far-UV radiation into molecular clouds". In: A&A 467.1, pp. 1–14. DOI: 10.1051/0004-6361:20066119.

Goicoechea, J. R. et al. (2016). "Compression and ablation of the photo-irradiated molecular cloud the Orion Bar". In: Nature 537.7619, pp. 207–209. DOI: 10.1038/nature18957.

Gonzalez Garcia, M. et al. (2008). "Radiative transfer revisited for emission lines in photon dominated regions". In: A&A 485.1, pp. 127–136. DOI: 10.1051/0004-6361:200809440.

Gould, R. J. and Salpeter, E. E. (1963). "The Interstellar Abundance of the Hydrogen Molecule. I. Basic Processes." In: ApJ 138, p. 393. DOI: 10.1086/147654.

Guzmán, V. et al. (2011). "H_2CO in the Horsehead PDR: photo-desorption of dust grain ice mantles". In: A&A 534, A49, A49. DOI: 10.1051/0004-6361/201117257.

Habart, E. et al. (2005). "Density structure of the Horsehead nebula photo-dissociation region". In: A&A 437.1, pp. 177–188. DOI: 10.1051/0004-6361:20041546.

Herbst, E. and van Dishoeck, E. F. (2009). "Complex Organic Interstellar Molecules". In: ARA&A 47.1, pp. 427–480. DOI: 10.1146/annurev-astro-082708-101654.

Hernández-Vera, C. et al. (2023). "The extremely sharp transition between molecular and ionized gas in the Horsehead nebula". In: A&A 677, A152. DOI: 10.1051/0004-6361/202347206.

Hollenbach, D. and Salpeter, E. E. (1971). "Surface Recombination of Hydrogen Molecules". In: ApJ 163, p. 155. DOI: 10.1086/150754.

Joblin, C. et al. (2018). "Structure of photodissociation fronts in star-forming regions revealed by Herschel observations of high-J CO emission lines". In: A&A 615, A129, A129. DOI: 10.1051/0004-6361/201832611.

Le Bourlot, J. et al. (2012). "Surface chemistry in the interstellar medium. I. H_2 formation by Langmuir-Hinshelwood and Eley-Rideal mechanisms". In: A&A 541, A76, A76. DOI: 10.1051/0004-6361/201118126.

Le Petit, F. et al. (2006). "A Model for Atomic and Molecular Interstellar Gas: The Meudon PDR Code". In: ApJS 164.2, pp. 506–529. DOI: 10.1086/503252.

Maillard, V. (2023). "Model of photo-evaporating fronts in star forming regions". Theses. Université Paris sciences et lettres.

Maillard, V., Bron, E., and Le Petit, F. (2021). "Dynamical effects of the radiative stellar feedback on the H I-to-H_2 transition". In: A&A 656, A65, A65. DOI: `10.1051/0004-6361/202140865`.

Marconi, A. et al. (1998). "Near infrared spectra of the Orion bar". In: A&A 330, pp. 696–710. DOI: `10.48550/arXiv.astro-ph/9710051`.

Mathis, J. S., Mezger, P. G., and Panagia, N. (1983). "Interstellar radiation field and dust temperatures in the diffuse interstellar medium and in giant molecular clouds". In: A&A 128, pp. 212–229.

Menten, K. M. et al. (2007). "The distance to the Orion Nebula". In: A&A 474.2, pp. 515–520. DOI: `10.1051/0004-6361:20078247`.

Pilbratt, G. L. et al. (2010). "Herschel Space Observatory. An ESA facility for far-infrared and submillimetre astronomy". In: A&A 518, L1, p. L1. DOI: `10.1051/0004-6361/201014759`.

Röllig, M. et al. (2007). "A photon dominated region code comparison study". In: A&A 467.1, pp. 187–206. DOI: `10.1051/0004-6361:20065918`.

Schlafly, E. F. et al. (2014). "A Large Catalog of Accurate Distances to Molecular Clouds from PS1 Photometry". In: ApJ 786.1, 29, p. 29. DOI: `10.1088/0004-637X/786/1/29`.

Tielens, A. G. G. M. and Hollenbach, D. (1985). "Photodissociation regions. I. Basic model." In: ApJ 291, pp. 722–746. DOI: `10.1086/163111`.

Wolfire, M. G., Vallini, L., and Chevance, M. (2022). "Photodissociation and X-Ray-Dominated Regions". In: *Annual Review of Astronomy and Astrophysics* 60.Volume 60, 2022, pp. 247–318. DOI: `https://doi.org/10.1146/annurev-astro-052920-010254`.

Wu, R. et al. (2018). "Constraining physical conditions for the PDR of Trumpler 14 in the Carina Nebula". In: A&A 618, A53, A53. DOI: `10.1051/0004-6361/201832595`.